PNAS
www.pnas.org

Supplementary Information for

Structural basis for recognition of RALF peptides by LRX proteins during pollen tube growth

Steven Moussu[1‡], Caroline Broyart[1‡], Gorka Santos-Fernandez[‡2], Sebastian Augustin[1], Sarah Wehrle[3], Ueli Grossniklaus[2], Julia Santiago[1*].

[1]The Plant Signaling Mechanisms Laboratory, Department of Plant Molecular Biology, University of Lausanne, 1015 Lausanne, Switzerland.
[2]Department of Plant and Microbial Biology and Zurich-Basel Plant Science Center, University of Zurich, 8008 Zurich, Switzerland.
[3]Institute of Bioengineering, École Polytechnique Fédérale de Lausanne, 1015 Lausanne, Switzerland.

[*]Corresponding author: julia.santiago@unil.ch (J.S)

[‡]These authors contributed equally to this work

This PDF file includes:

Figs. S1 to S22
Table S1 and S2

www.pnas.org/cgi/doi/10.1073/pnas.2000100117

Figure S1. RALF4/19 form a tight complex with the LRR core of pollen LRX proteins.

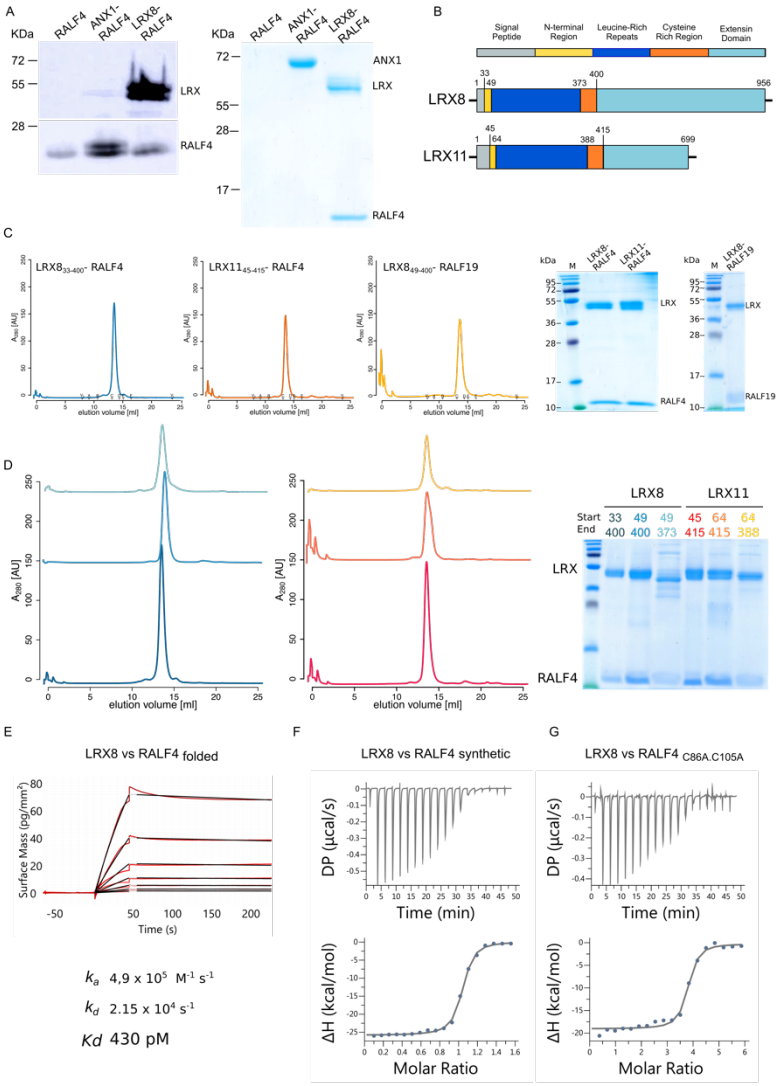

(*A*) Anti-HIS Western blot (left) of insect-cell culture pellets expressing or co-expressing RALF4, ANX1-RALF4 and LRX8-RALF4. SDS-PAGE of corresponding secreted protein fractions (right). (*B*) Schematic overview of LRX8 and LRX11 domains, including the amino acid coordinates according to structural data. (*C*) Analytical size exclusion chromatography (SEC) of $LRX8_{33\text{-}400}$-RALF4, $LRX11_{45\text{-}415}$-RALF4, and $LRX8_{49\text{-}400}$-RALF19 complexes (left). SDS-PAGE (right) of the different peaks corresponding to the SEC experiments. (*D*) Mapping of the LRX8/LRX11 domain interacting with RALF4 according to the schematic diagram in (*B*). SEC (left) of the LRX8/11-RALF4 complexes. SDS-PAGE (right) of the different SEC peaks. Colors of the SEC plots and the corresponding peak legends are matching. (*E*) Grating-coupled interferometry (GCI)-derived binding kinetics for LRX8 *vs* $RALF4_{folded}$. Shown are the sensogram with data in red and the respective curve fits in black. Table summaries of kinetic parameters are shown below (k_a, association rate constant; k_d, dissociation rate constant; K_D, dissociation constant). (*F*) and (*G*) Isothermal titration calorimetry thermogram (ITC) of the LRX8 protein *vs* $RALF4_{synthetic}$ and $RALF4_{C86A.C105A}$, respectively.

Figure S2. LRX8-RALF4 and LRX11-RALF4 mass spectrometry sequence determination.

A

B

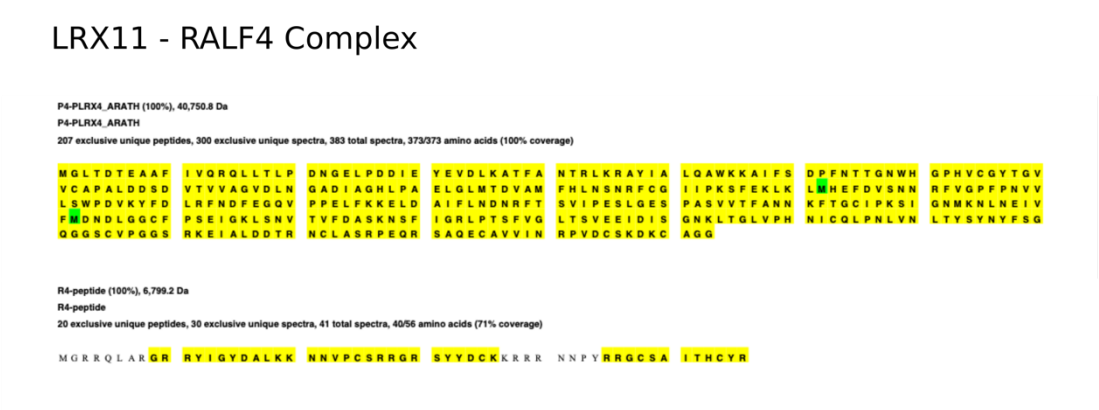

C

(A) and *(B)* Results from LC-MS/MS analysis of LRX8-RALF4 and LRX11-RALF4 protein complexes. Number of peptides and coverage for each component of the complex is highlighted in yellow. Oxidised methionines are highlighted in green. Leu 3 of LRX8 was identified as the N-terminal, N-acetylated residue, although the modification was only sporadically identified and was thus partial. Cys residues were reduced and alkylated (carbamidomethyl, not shown) and searched as fixed modification. All the sequence coverages are the combined results of tryptic and chymotryptic digestions and separate LC-MS/MS analyses on a high resolution orbitrap Fusion instrument. Samples in (*A*) were analysed by both HCD and EThcD fragmentation, while for results in (*B*) only HCD fragmentation was used. For more details see the Materials and Methods section. *(C)* Sequence map of full length RALF4 indicating the amino acid coordinates corresponding to the different signatures of the protein.

Figure S3. Isothermal titration calorimetry assays of LRX8 *vs* RAL4$_{folded}$, RALF4$_{CCCC}$ and RALF4$_{sythetic}$.

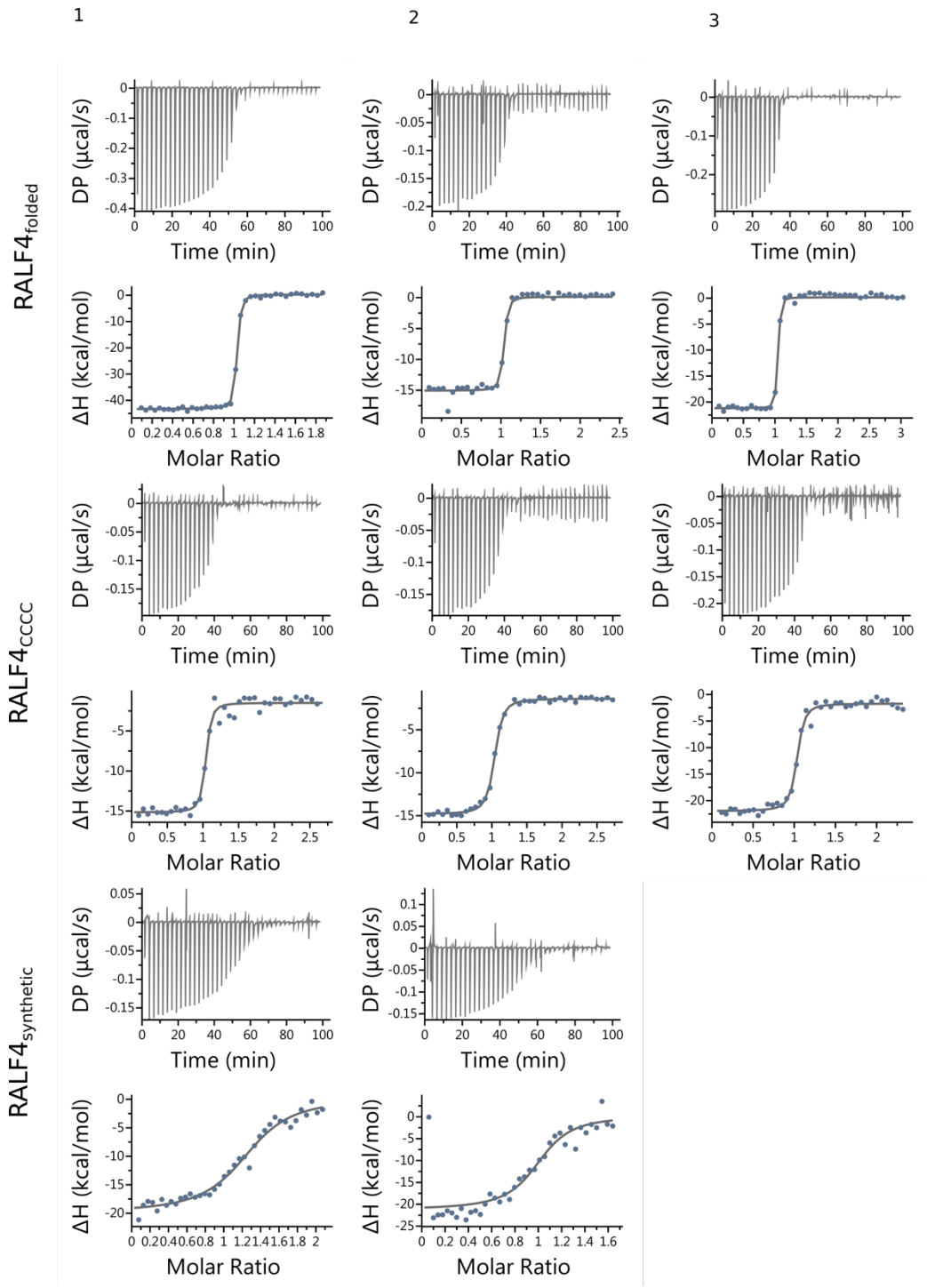

ITC thermograms of the independent experiments performed for each peptide.

Figure S4. Near-UV Circular Dichroism on different RALF4 peptides.

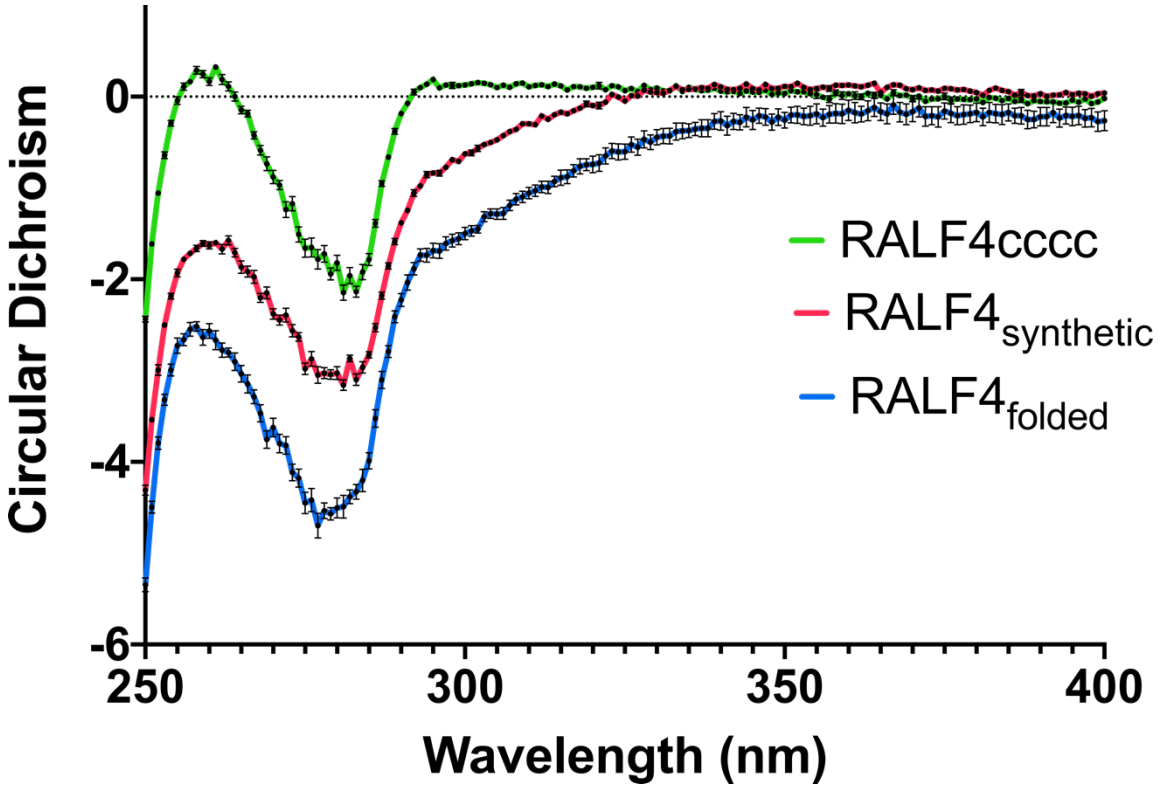

Circular dichroism near-UV spectra corresponding to different RALF4 peptides in solution. Depicted are the spectra for $RALF4_{folded}$ (blue), $RALF4_{synthetic}$ (red) and $RALF4_{CCCC}$ (green). Broad increase in signal (y-axes) indicates an increase in disulfide bonds abundance. Error bars represent the SEM over 10 measures.

Figure S5. LRX8 and 11 are constitutive dimers in their apo form or in complex with RALF4.

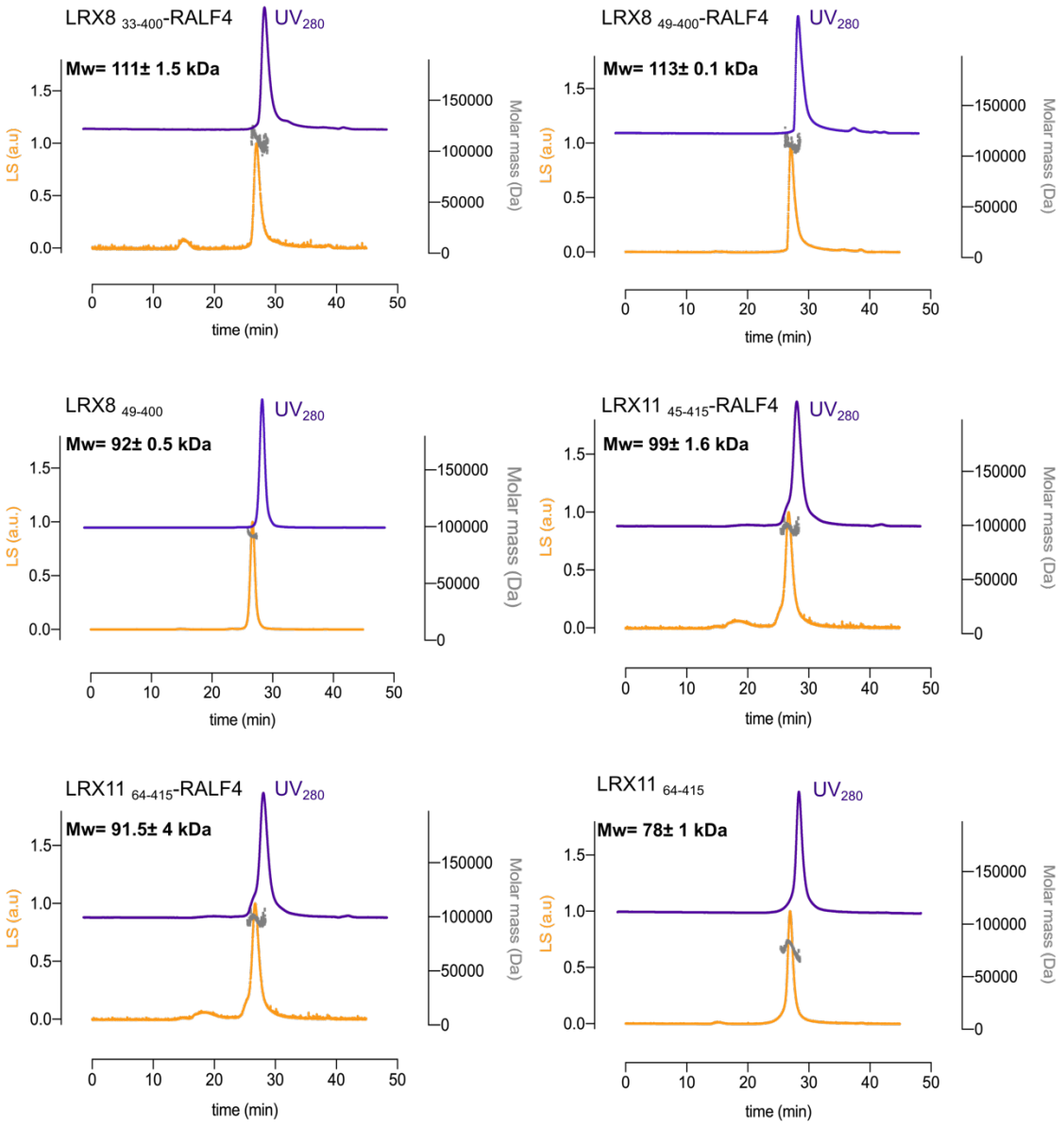

Molecular weight determination of the respective complexes using Multi Angle Light Scattering (MALS). UV_{280} absorption is plotted in purple, light scattering (LS) in orange, and the determined molecular weight (Da) in grey. The molecular weight indicated on each plot is the mean ± SD of two independent measurements.

Figure S6. LRX8-RALF4 and LRX2-RALF4 complexes share a common architecture.

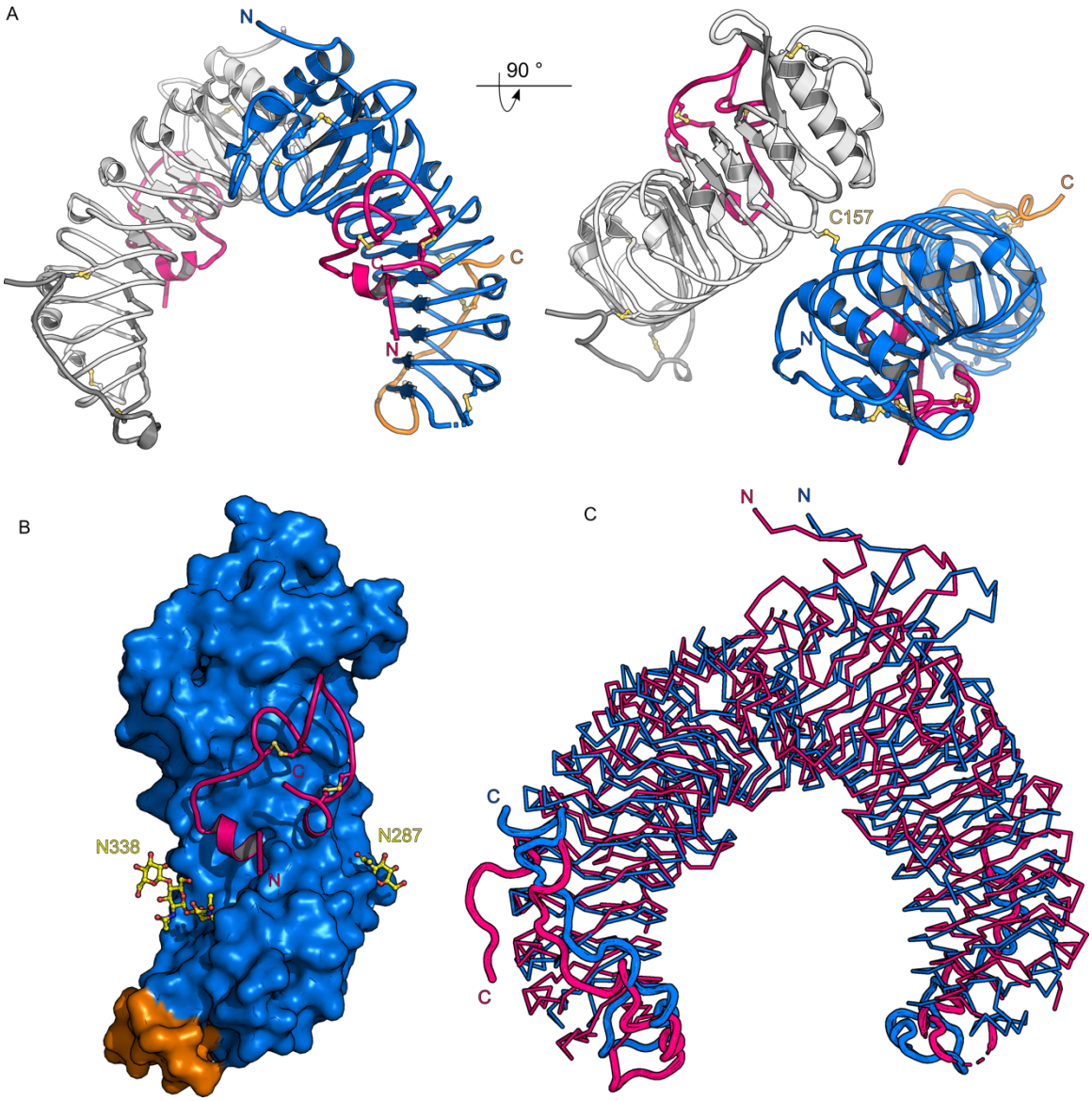

(*A*) Front and 90º x-axis rotated view of LRX8 covalently linked homodimer in complex with RALF4 (ribbon diagram). The LRR domain is depicted in blue, the Cys-rich tail in orange, and the RALF4 peptide is highlighted in pink. The disulfide bridge covalently linking the two LRX protomers is highlighted in yellow. (*B*) Surface view of LRX8 (color code as in *A*) along with cartoon representation of RALF4 peptide (in pink), highlighting the binding surface of the peptide. N-glycosylations are depicted in yellow. (*C*) Structural superimposition of the LRX2-RALF4 (Cα trace in pink) and LRX8-RALF4 (in blue) complexes. r.m.s.d. of ~ 0.8 Å comparing 357 pairs of corresponding Cα atoms between LRX2-RALF4 and LRX8-RALF4 complexes.

Figure S7. The LRX2/8-RALF4 complex interfaces are conserved among the LRX protein family.

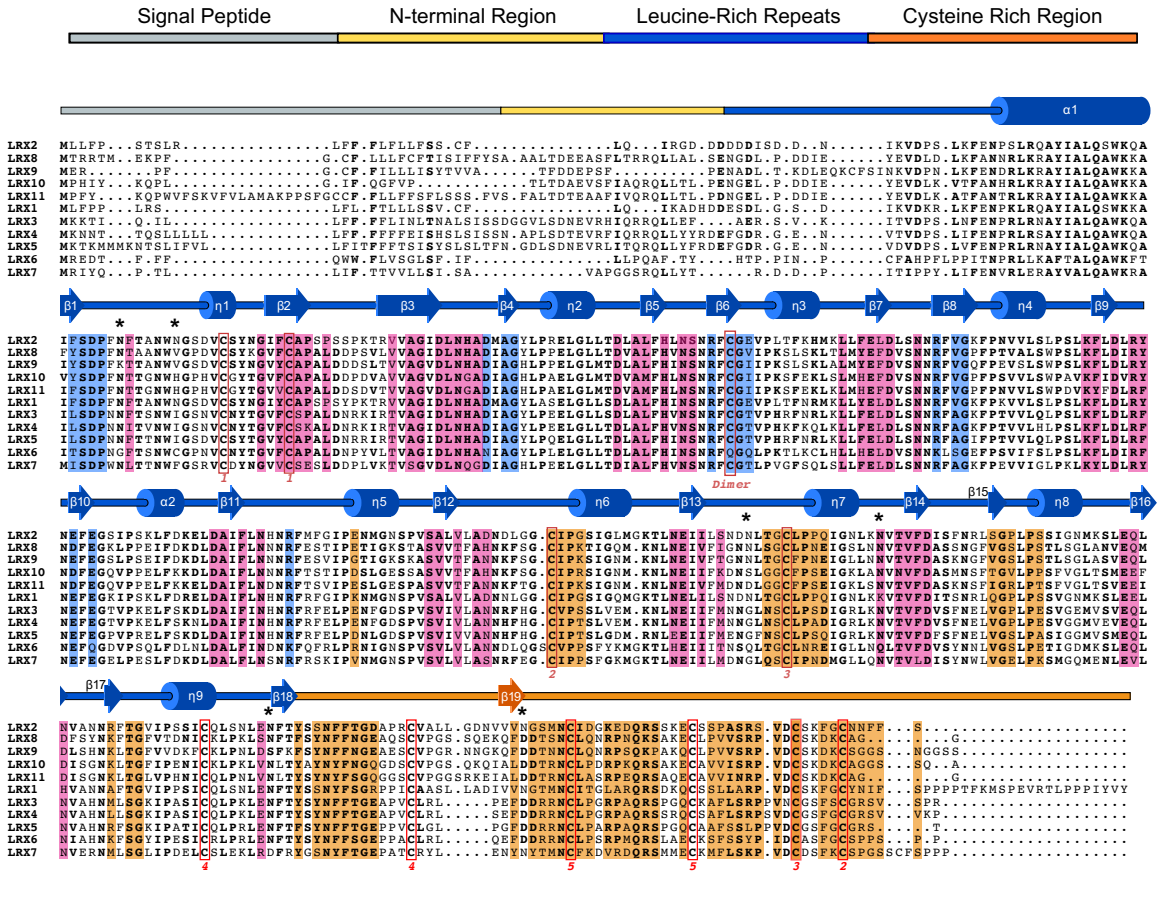

Structure-based sequence alignment of the LRX family members. The alignment includes a secondary structure assignment calculated with the program DSSP and colored according to Fig. 2 and Fig. S1*B*. Cys residues engaged in disulfide bonds are squared in red, with matching pairs indicated by numbers. Predicted and experimentally verified N-glycosylation sites are depicted by black stars. The various interaction surfaces in the LRX2/8-RALF4 complex structures are highlighted according to the following color code: LRX dimer interface in blue, LRX-RALF4 binding pocket in pink, and the interaction surface of the LRX Cys extension with the LRR core of the protein is highlighted in light orange.

Figure S8. RALF4 omit map and surface electrostatic potential of the peptide exposed surface.

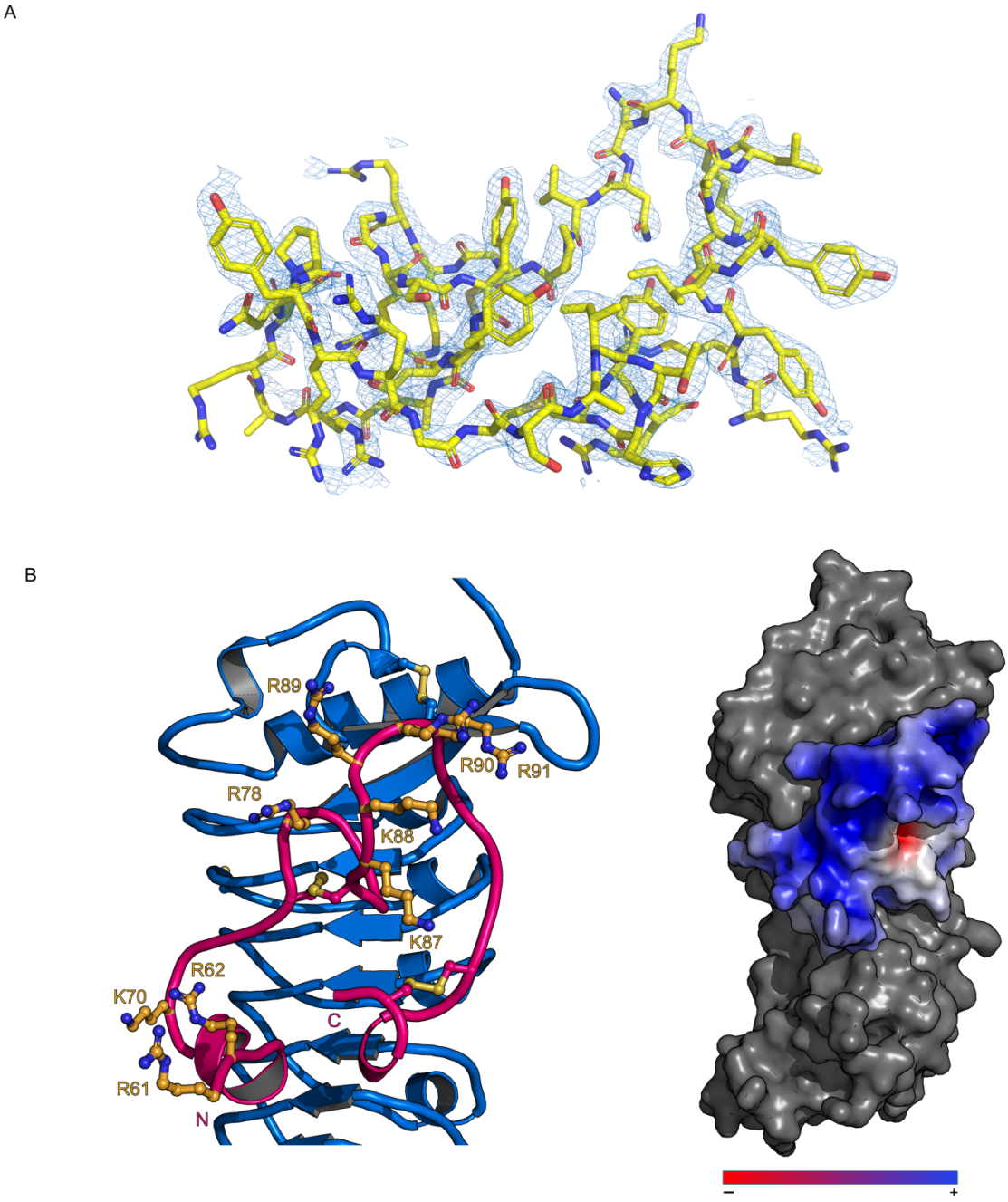

(*A*) RALF4 simulated annealing 2Fo-Fc omit electron density map contoured at 1.5 σ. (*B*) RALF4 reveals a positively-charged surface when bound to LRX. Details of the basic nature of RALF4 exposed surface (left). Arg (R) and Lys (K) free residues are shown as sticks in light orange. Electrostatic surface representation of RALF4 when in complex with LRX2 (right). LRX2 is shown in grey and RALF4 solvent-accessible surface electrostatic potential has been calculated using APBS plugin (PyMOL). The potential is given with the negative (red) and positive (blue) contour levels in the range from -8.0 to +8.0 kBT, respectively.

Figure S9. RALF4 binding interface to LRX is conserved among closely related RALF family members.

A

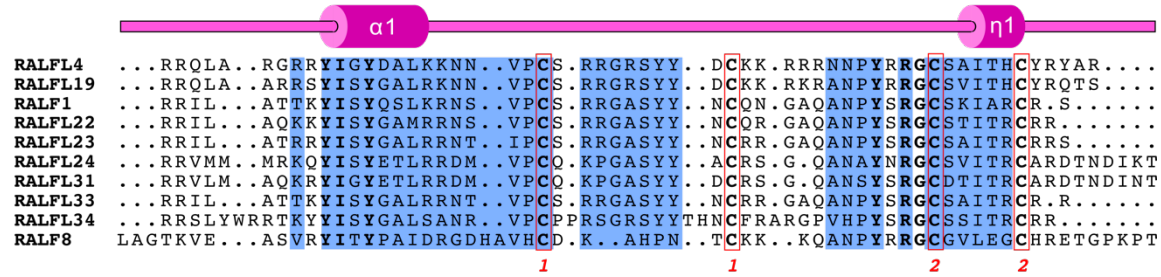

B

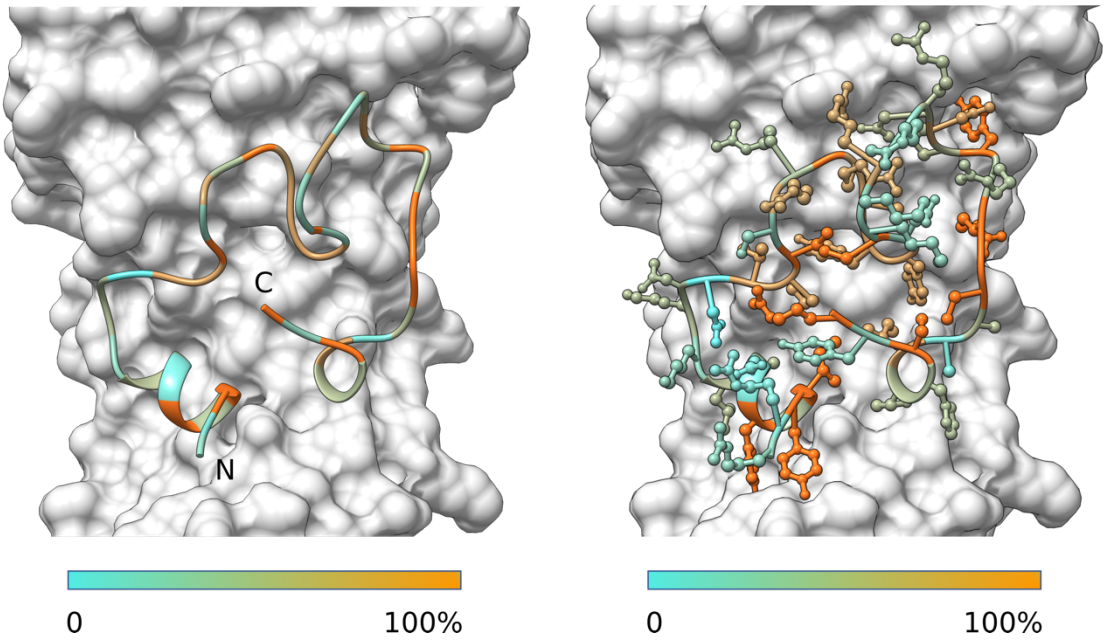

(*A*) Structure-based sequence alignment of RALF4 family related members. The alignment includes a secondary structure assignment calculated with the program DSSP and colored according to Fig. 2. Cys residues engaged in disulfide bonds are squared in red, with matching pairs indicated by numbers. The RALF4-LRX2 interaction surface is highlighted in blue. (*B*) The RALF4 regions directly interacting with the LRX binding pocket (highlighted in blue above) are conserved among RALF4-related family members. RALF4 ribbon representation (left) and depicting the amino acid lateral-chains (right) colored according to sequence conservation among RALF peptides indicated in the alignment above.

Figure S10. Ligplot representation of the interactions occurring in the LRX8-RALF4 interface.

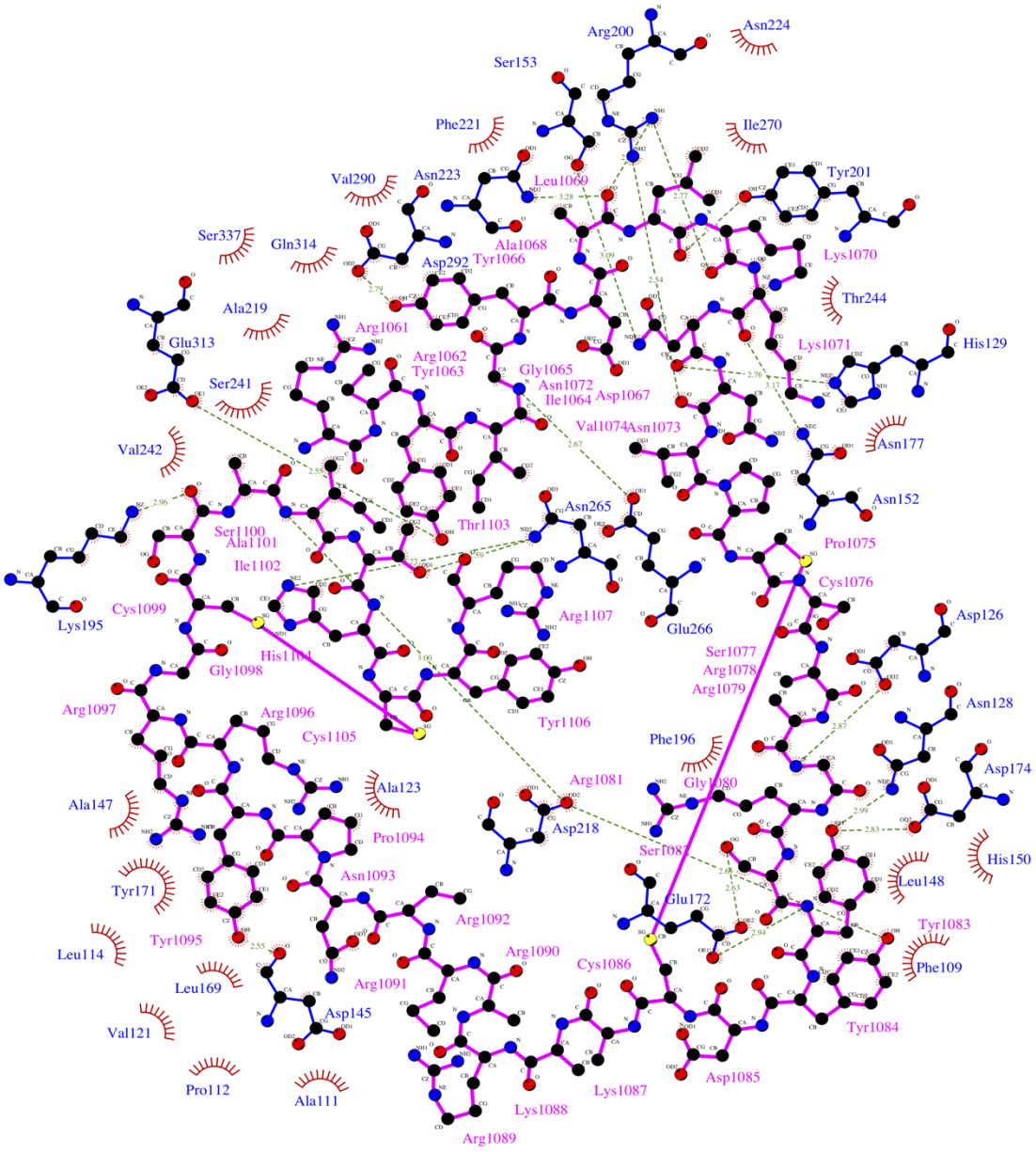

2-D ligand-interaction diagram of RALF4 (pink) and LRX8 (blue) generated with Ligplot. Hemispheres represent hydrophobic interactions. Disulfide bonds are depicted with a pink solid line and hydrogen bonds are represented in green.

Figure S11. *In vitro* and *in vivo* validation of the LRX8-RALF4 structure complex.

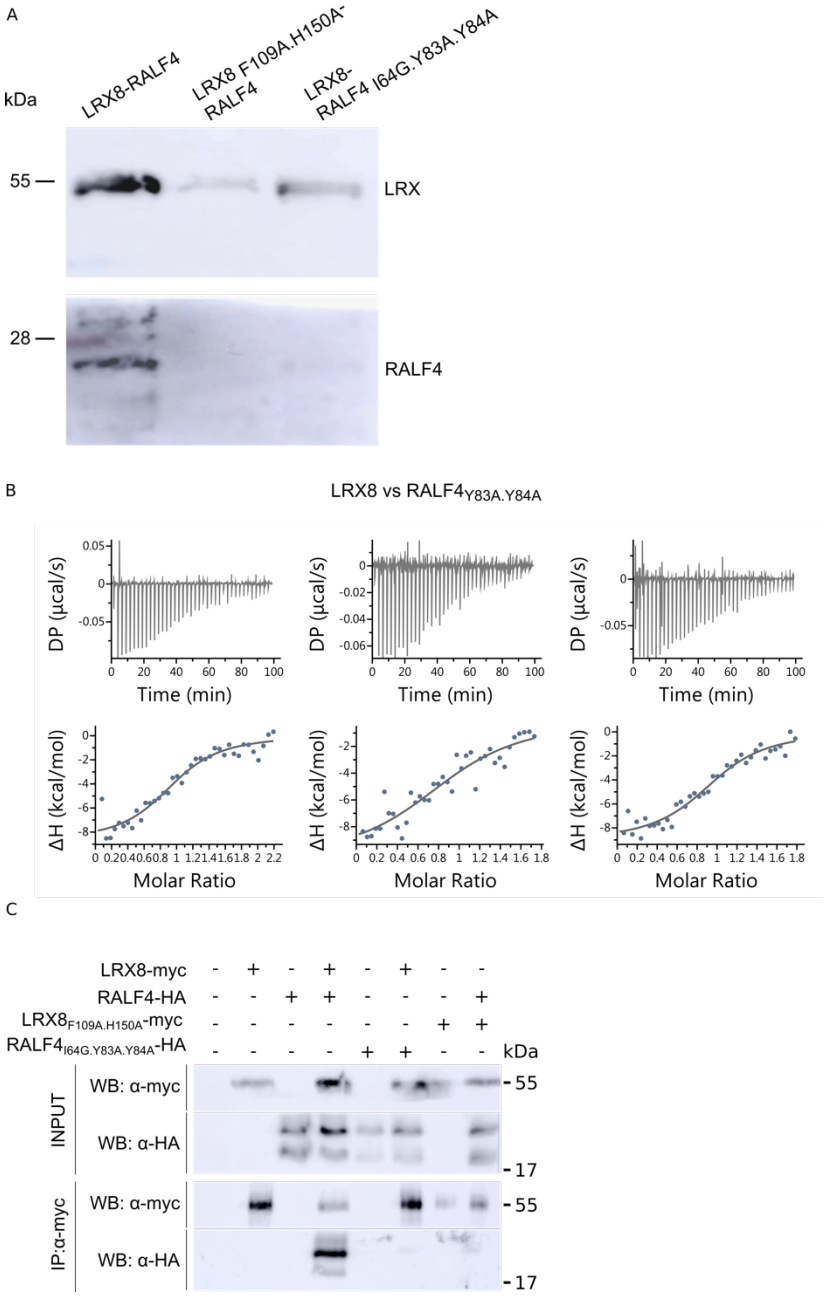

(*A*) *In vitro* validation of the LRX8-RALF4 complex. Western blot from insect cell co-expression cultures of LRX8-RALF4, LRX8$_{F109A.H150A}$-RALF4 (LRX peptide binding-pocket mutant), and LRX8-RALF4$_{I64A.Y83A.Y84A}$ (peptide binding mutant). (*B*) ITC thermograms of LRX8 *vs* RALF4$_{Y83A.Y84A}$. (C) *In vivo* validation of the LRX8-RALF4 complex structure. Co-immunoprecipitation (Co-IP) of LRX8-myc and RALF4-HA proteins transiently expressed in tobacco were performed using an anti-myc antibody (IP:α-myc). RALF4-HA peptides were detected with an anti-HA antibody in the IP elution.

Figure S12. Characterization of LRX8 complementation lines.

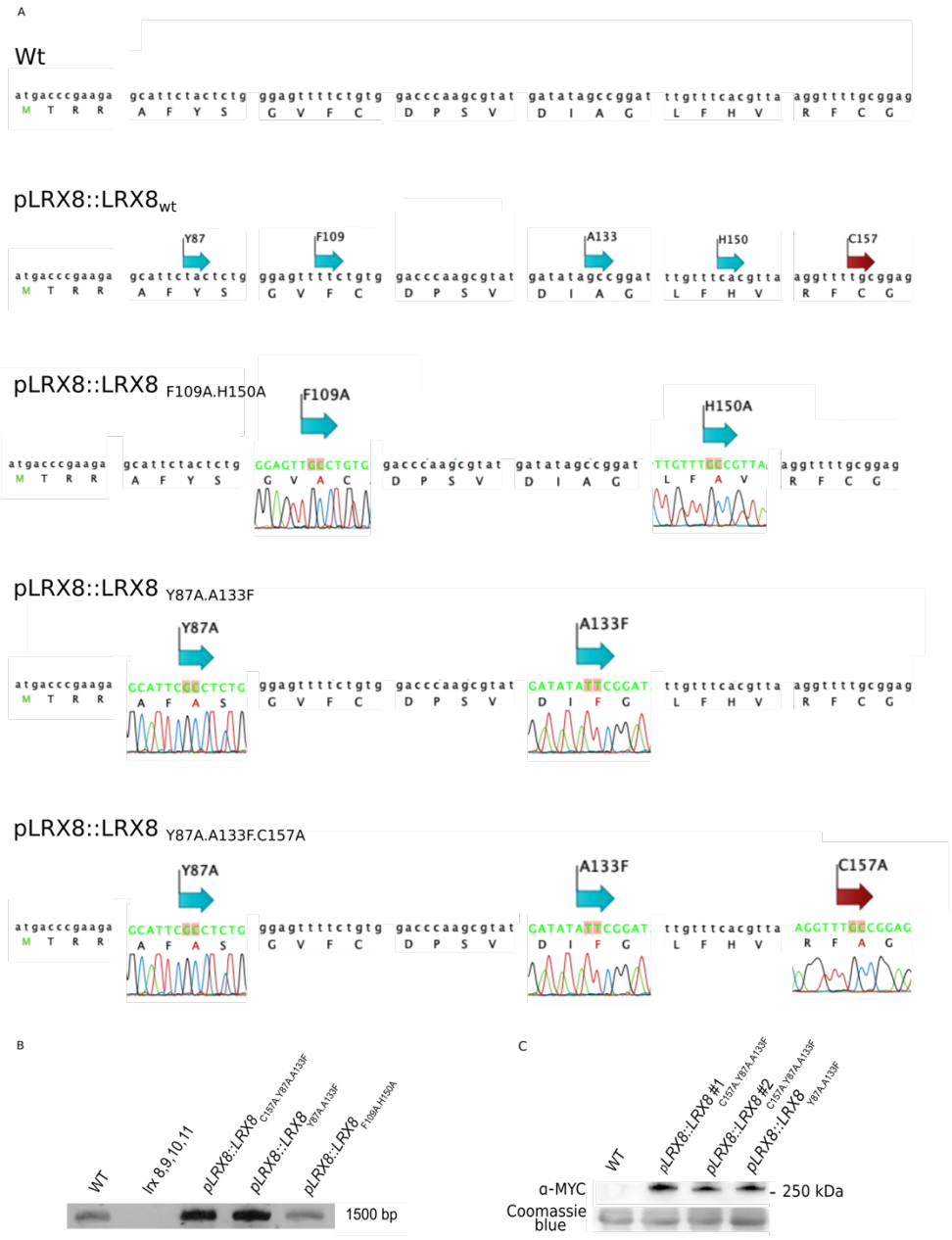

(*A*) Sequencing data of cDNA amplification of LRX8 in WT and *lrx8,9,10,11* complemented with either *pLRX8::LRX8*$_{C157A.Y87A.A133F}$, *pLRX8::LRX8*$_{Y87A.A133F}$ or *pLRX8::LRX8*$_{F109A.H150A}$, showing that the expression of the LRX8 band in (*B*) corresponds to the expression of the inserted mutant versions. (*B*) cDNA amplification of LRX8 in WT, *lrx8,9,10,11*, and *lrx8,9,10,11* complemented by either *pLRX8::LRX8*$_{C157A.Y87A.A133F}$, *pLRX8::LRX8*$_{Y87A.A133F}$, or *pLRX8::LRX8*$_{F109A.H150A}$, showing restoration of LRX8 expression in the complemented lines. (*C*) α-myc protein detection of LRX8 mutants in pollen.

Figure S13. *In planta* cell wall localization of LRX8 wild type and oligomeric mutants.

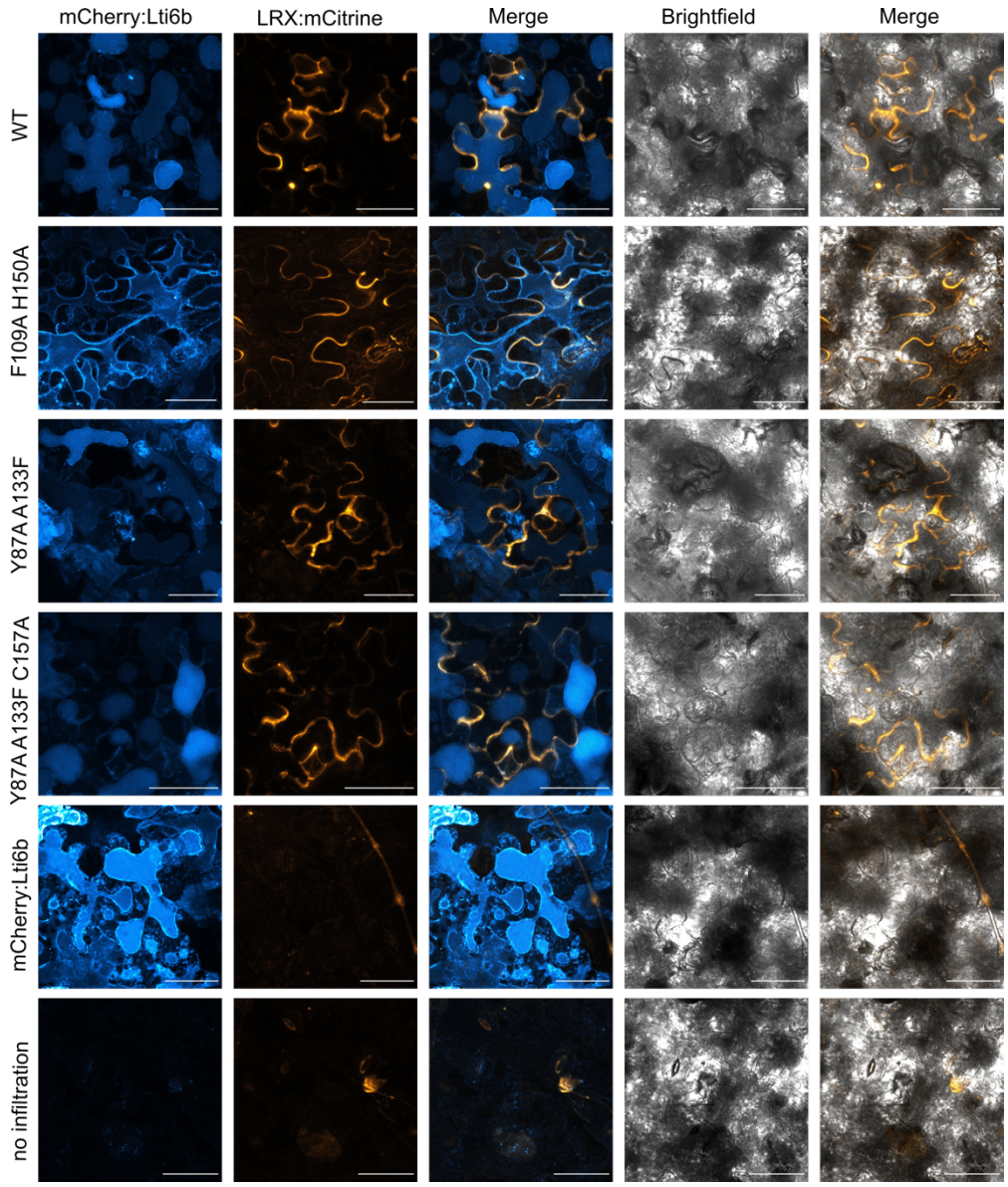

Subcellular localization of LRX8-mCitrine mutants. Plasmolysis experiments were performed on *N. benthamiana* leaves transiently transformed with mCitrine tagged LRX8 WT and mutants: *LRX8*$_{F109A.H150A}$-mCitrine, *LRX8*$_{Y87A.A133F}$-mCitrine, *LRX8*$_{C157A.Y87A.A133F}$-mCitrine, to check for proper cell wall localization. mCherry-Lti6b plasma membrane marker, depicted in blue, is used to properly visualize the shrinking of plasma membrane upon plasmolysis. The last two rows represent controls with only the plasma membrane marker or no infiltrated samples. Scale bar = 50 µm.

Figure S14. Purified proteins used in ITC experiments and ITC binding matrix of LRX8 and LRX8-RALF4$_{folded}$ *vs* pollen *Cr*RLK1L and LLGs.

A

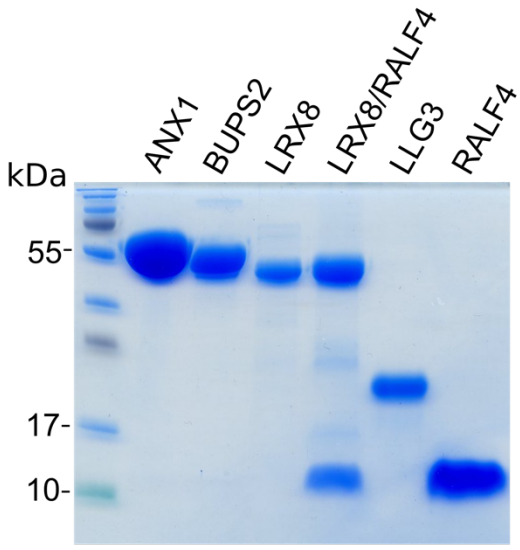

B

Ligand (Syringe)	Protein (Cell)	pH	Kd (nM)	ΔH (kcal/mol)	N
ANX1	LRX8	5		no binding detected	
BUPS2	LRX8	5		no binding detected	
LRX8	LLG3	5		no binding detected	
ANX1	LRX8-RALF4	5		no binding detected	
BUPS2	LRX8-RALF4	5		no binding detected	
LRX8-RALF4	LLG3	5		no binding detected	

Ligand (Syringe)	Protein (Cell)	pH	Kd (nM)	ΔH (kcal/mol)	N
ANX1	LRX8	7.5		no binding detected	
BUPS2	LRX8	7.5		no binding detected	
LRX8	LLG3	7.5		no binding detected	
ANX1	LRX8-RALF4	7.5		no binding detected	
BUPS2	LRX8-RALF4	7.5		no binding detected	
LRX8-RALF4	LLG3	7.5		no binding detected	

(*A*) SDS-PAGE of the purified proteins used in the ITC binding matrix. (*B*) ITC binding matrix of LRX8 and LRX8-RALF4 complex *vs Cr*RLK1L and LLGs in alkaline and acidic conditions.

Figure S15. Isothermal titration calorimetry thermograms of RALF4$_{folded}$ and LRX8 *vs* *Cr*RLK1Ls/LLGs at pH 7.5.

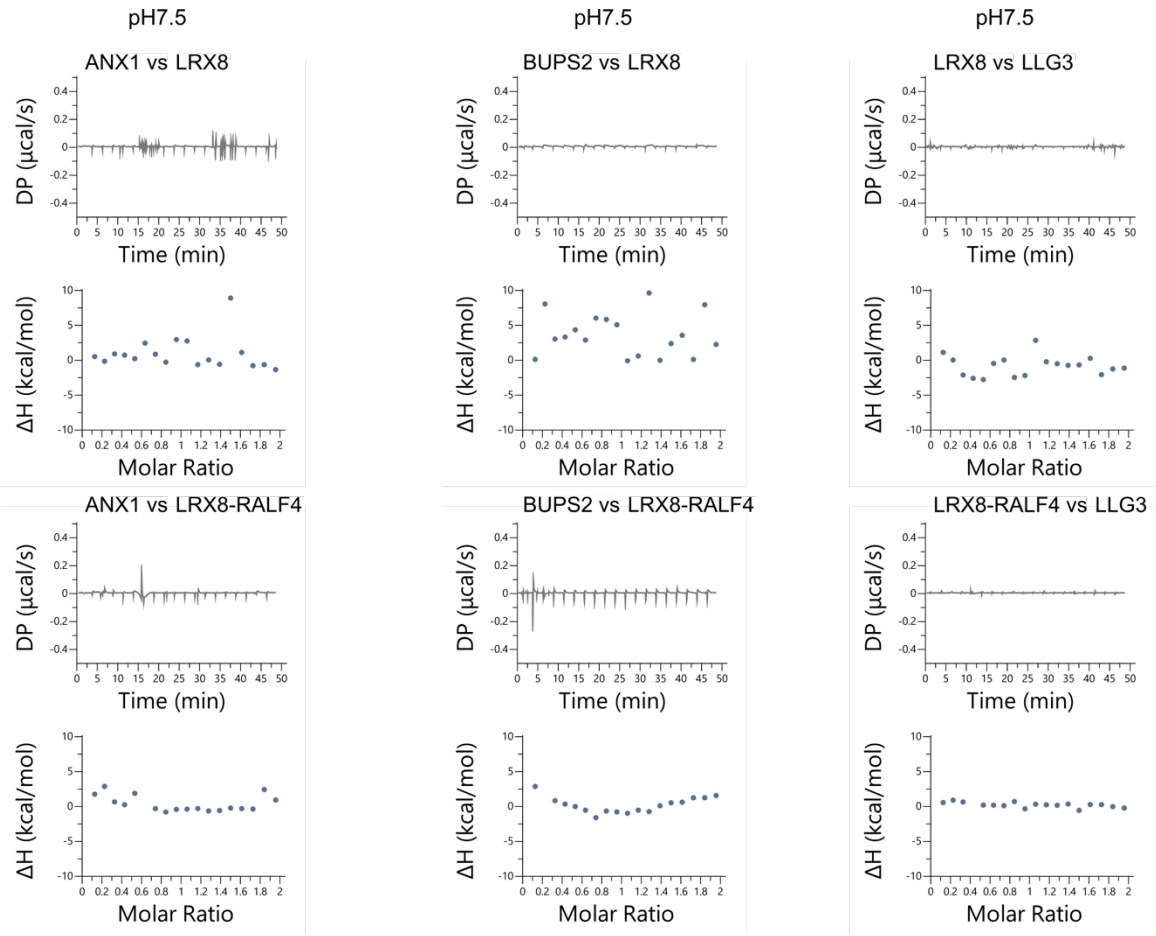

ITC thermograms of the independent experiments analyzed in Fig. S14B at pH 7.5.

Figure S16. Isothermal titration calorimetry thermograms of RALF4$_{folded}$ and LRX8 *vs* *Cr*RLK1Ls/LLGs at pH 5.

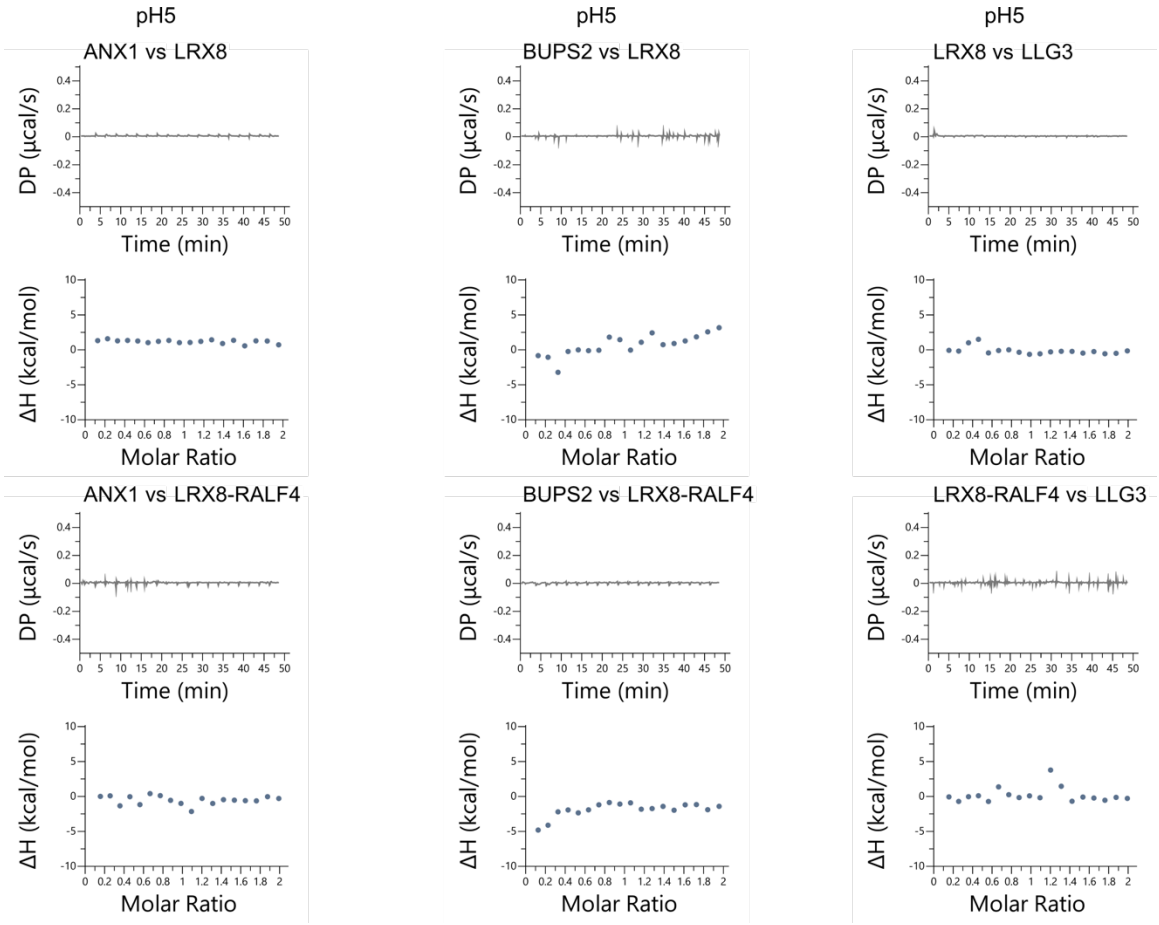

ITC thermograms of the independent experiments analyzed in Fig. S14B at pH 5.

Figure S17. Isothermal titration calorimetry thermograms of LRX8 and LLGs *vs* RAL4$_{folded}$ in alkaline and acidic conditions.

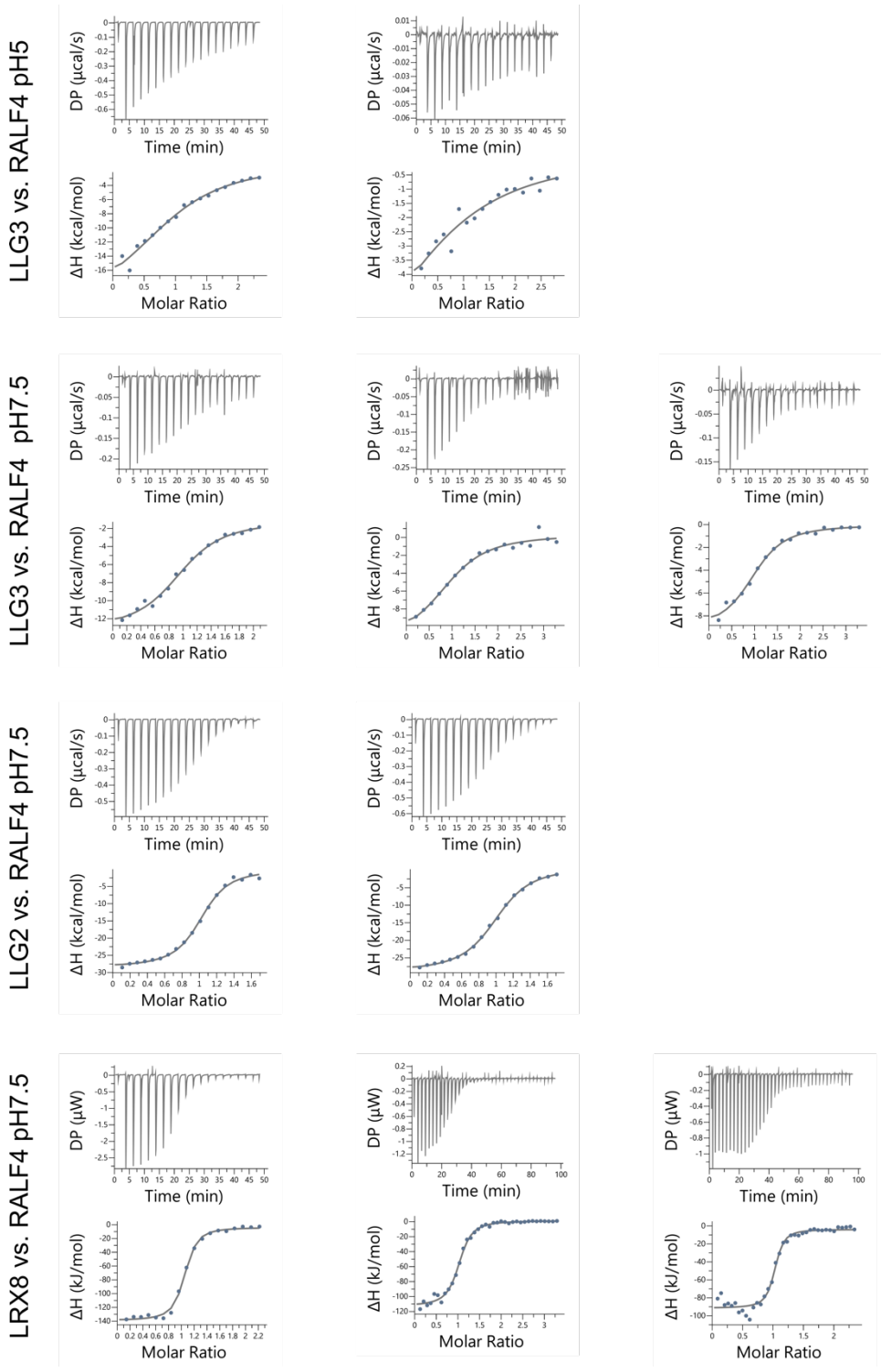

ITC thermograms of the independent experiments analyzed in Fig. 3*F*

Figure S18. Isothermal titration calorimetry thermograms of LRX8 and LLG3 *vs* RAL4$_{folded}$ Y63AY66A mutant in acidic conditions and alkaline conditions.

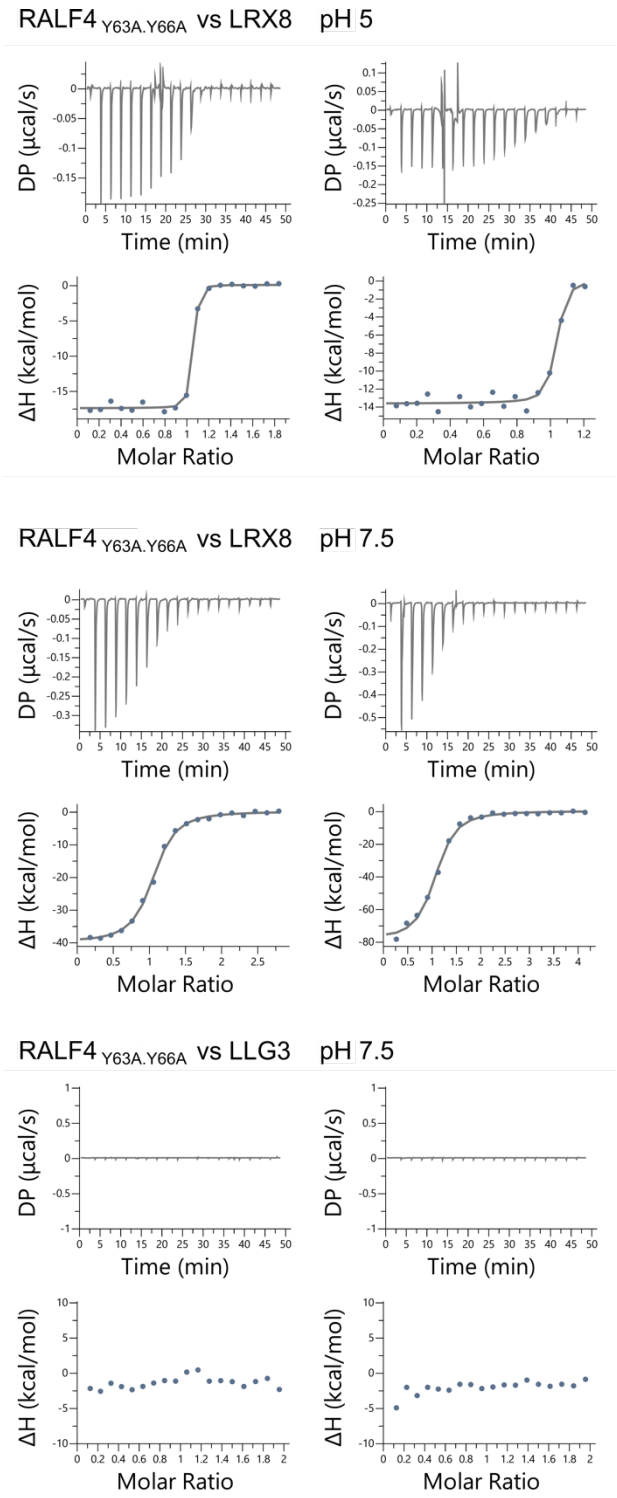

ITC thermograms of the independent experiments analyzed in Fig. 3*F*

Figure S19. Quantitative SEC-MALS analysis of the LRX-RALF dimer interface mutants and binding analysis of RALF4 to LRX8 monomer.

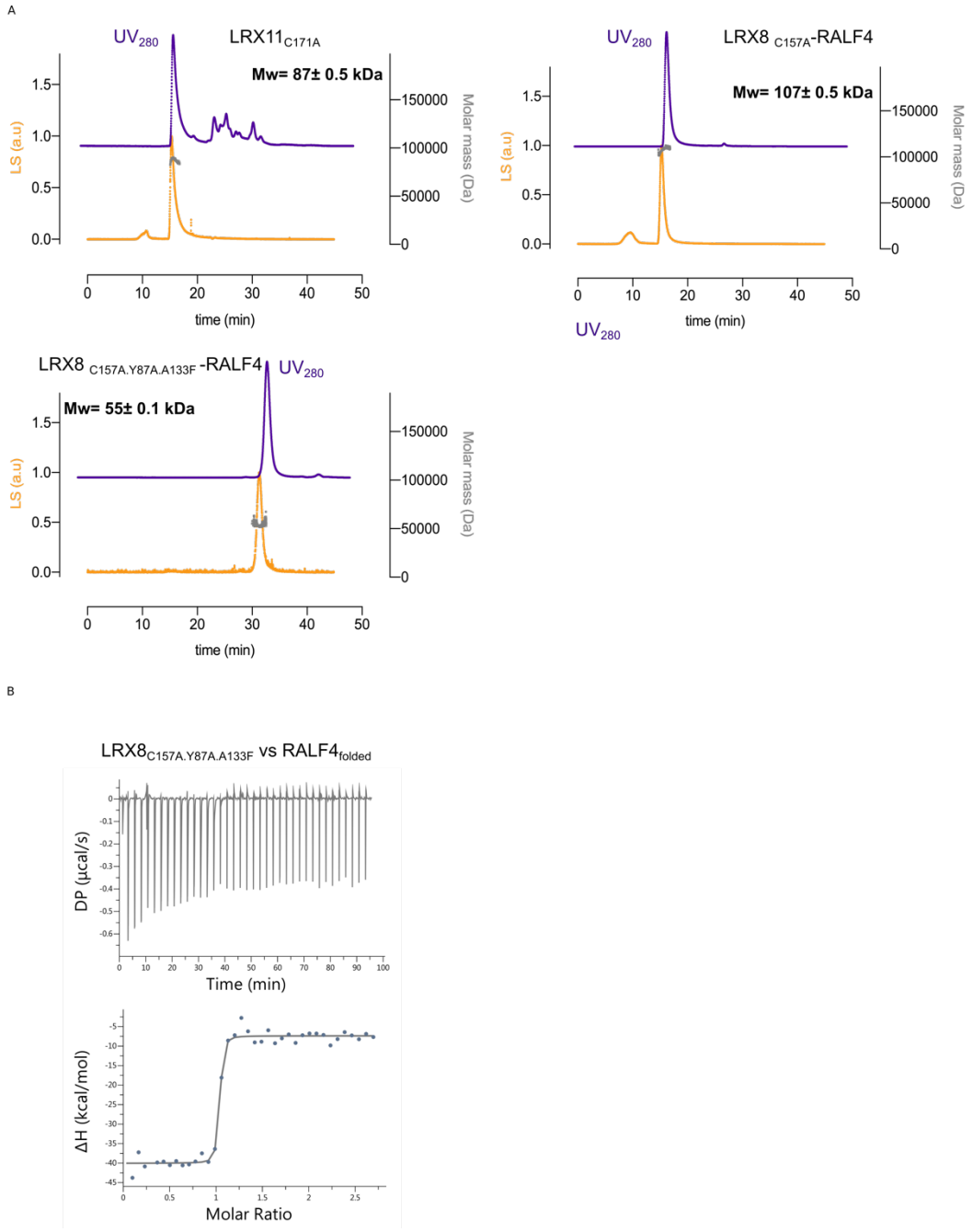

(*A*) Molecular weight determination of the respective complexes using MALS. UV_{280} absorption is plotted in purple, light scattering (LS) in orange, and the determined molecular weight (Da) in grey. The molecular weight indicated on each plot is the mean ± SD of two independent measurements. (*B*) ITC thermogram of $RALF4_{folded}$ *vs* $LRX8_{C157A.Y87A.A133F}$.

Figure S20. Monomeric LRX8 in complex with RALF4 shares a common architecture with the wild-type dimeric complex.

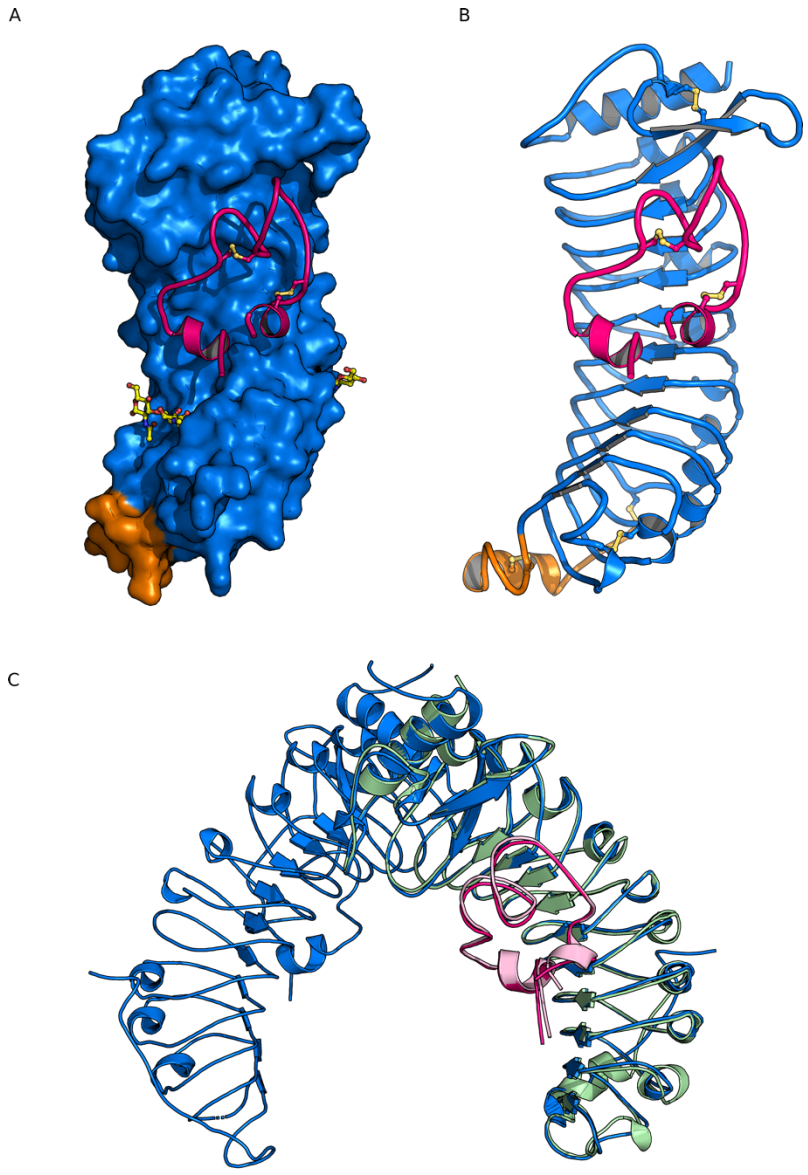

(*A*) Surface view of LRX8 (color code as in Fig. 2) along with cartoon representation of RALF4 peptide (in pink), highlighting the binding surface of the peptide. N-glycosylations are depicted in yellow. (*B*) Front view of LRX8 monomer in complex with RALF4 (ribbon diagram). The LRR domain is depicted in blue, the Cys-rich tail in orange, and the RALF4 peptide is highlighted in pink. (*C*) Structural superimposition of the LRX8-RALF4 dimer (Cα trace in blue, with the peptide in pink) and LRX8-RALF4 monomer (Cα trace in green, with the peptide depicted in light pink) complexes. R.m.s.d. of ~ 0.65 Å comparing 327 corresponding Cα atoms between the two proteins.

Figure S21. *In vivo* and *in vitro* confirmation of disulfide bonded LRX8 dimers.

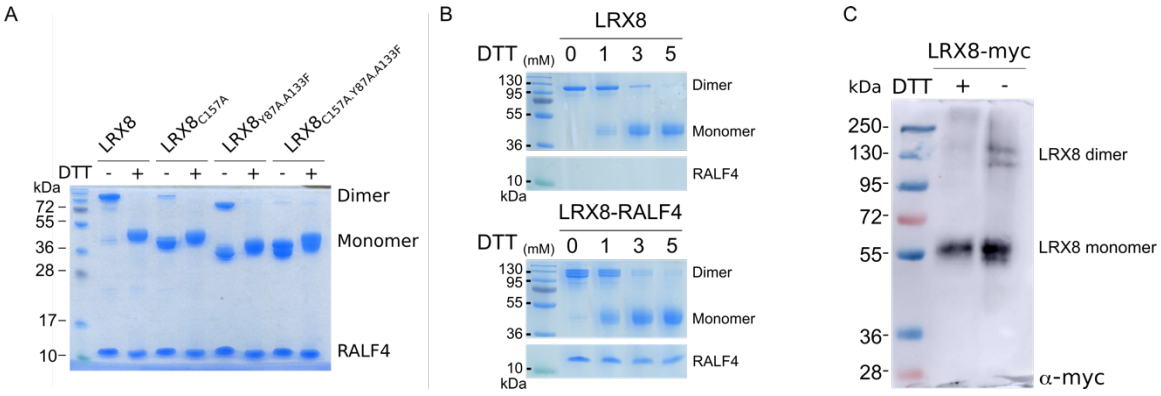

(A) SDS-PAGE analysis in the presence/absence of DTT of the mutants shown in Fig 4*C*. (*B*) *In vitro* validation of covalently linked LRX8 homodimers in denaturing conditions. SDS-PAGE gels of LRX8 alone (left) and in complex with RALF4 (right), treated with increasing DTT concentrations (0, 1, 3, and 5 mM). Dimers run above 100kDa while monomers run around 50kDa. (*C*) Detection of monomer and dimer species of transiently expressed $LRX8_{1\text{-}400}$ in tobacco leaves, ± DTT.

Figure S22. Dominant active MRI$_{R240C}$ does not suppress the mutant phenotype of multiple *lrx* mutants.

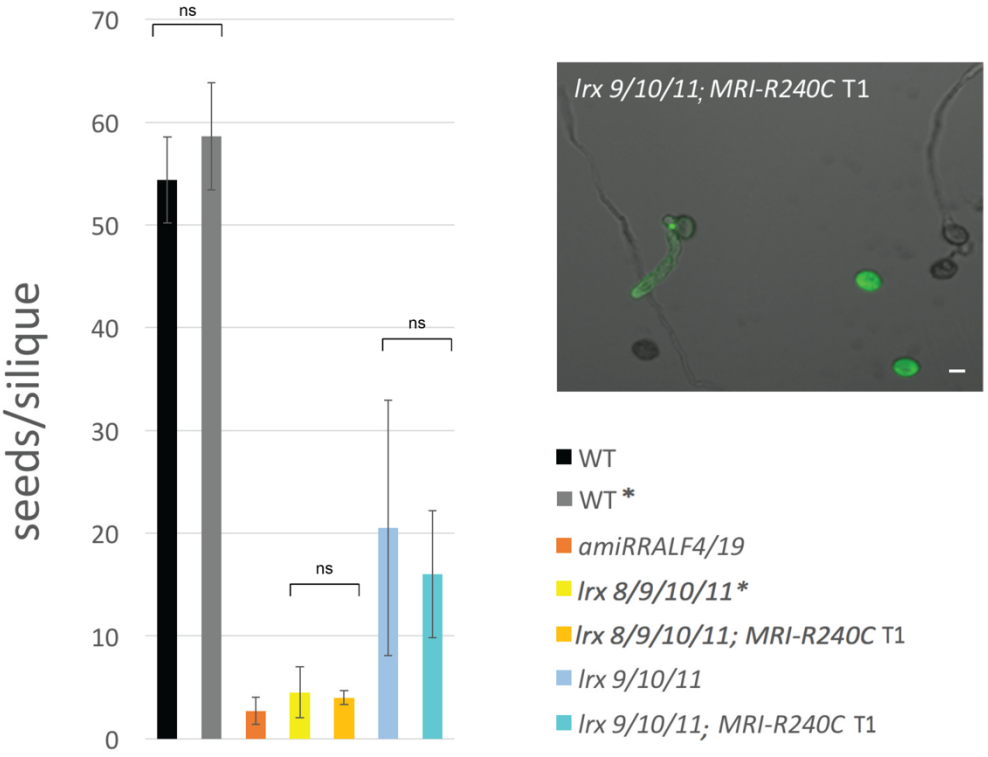

Introduction of the dominant active MRI$_{R240C}$ kinase does not suppress the pollen tube defects of *lrx8/9/10/11* quadruple and *lrx9/10/11* triple mutants, as evidenced by the strongly reduced seed set per silique. Mutants with or without the MRI$_{R240C}$ transgene (3 independent T1 lines) show no statistically significant (ns) difference in seed set. Six to eight siliques of three plants were analyzed per genotype. The plants marked by * were not grown at the same time (data from ref[5]) but since the wild-type (wt) controls showed no statistically significant difference, they are shown in the same graph. The inlet shows that although MRI$_{R240C}$-CFP was expressed in pollen grains and pollen tubes of the T1 plants, it did not suppress the *lrx9/10/11* mutant phenotype. Scale bar, 10 μm.

Table S1. Crystallographic data-collection and refinement statistics.

	LRX2-RALF4 *native*	**LRX8-RALF4** *native*	**LRX8$_{monomer}$-RALF4** *native*
Data collection			
Space group	*P 41*	*C 1 2 1*	*P1*
Cell dimensions			
a, *b*, *c* (Å)	119.99, 119.99, 305.73	205.84, 114.09, 146.97	51.8, 65.54, 83.7
α, β, γ (°)	90, 90, 90	90, 116.25, 90	72.12, 87.62, 68.36
Resolution (Å)	59.99 – 3.20 (3.31 – 3.20)	49.44 – 3.89 (4.13 – 3.89)	48 – 2.33 (2.47-2.33)
R_{meas}[#]	0.413 (2.79)	0.457 (2.15)	0.149 (1.02)
CC(1/2)[#] *(%)*	99.7 (58.1)	97.8 (34.8)	99 /42.5)
$I/\sigma I$[#]	10.82 (1.33)	4.44 (1.06)	5.21(1.14)
Completeness (%)[#]	99.82 (99.49)	99.6 (99.2)	97.2 (90.6)
Redundancy[#]	26.66 (27.55)	6.7 (6.7)	1.8 (1.77)
Wilson B-factor[#]	78.54	93.85	34.6
Refinement			
Resolution (Å)	59.99 – 3.20 (3.31 – 3.20)	49.44 – 3.89 (4.13 – 3.89)	48-2.33 (2.47-2.33)
No. reflections	1,212,145 (184,586)	191,042 (30,086)	142,294 (78,713)
R_{work}/ R_{free}[$]	0.223/0.272 (0.370/0.424)	0.281/0.329 (0.326/0.379)	0.172/0.228 (0.251/0.319)
No. atoms			
Protein	23,520	14,844	5,752
Glycan	773	226	84
R.m.s deviations[$]			
Bond lengths (Å)	0.003	0.003	0.008
Bond angles (°)	0.75	0.76	0.9
Molprobity results			
Ramachandran outliers (%)[‡]	0.27	0.32	0.00
Ramachandran favored (%)[‡]	90.62	87.54	92.63
Molprobity score[‡]	2.16	2.22	1.74
PDB-ID	**6QXP**	**6QWN**	**6TME**

(#) XDS (54), ($) PHENIX (49), (‡) MOLPROBITY (52)

Table S2. Correspondence between amino acids of LRX2, LRX8, and LRX11.

Surface	LRX2	LRX8	LRX11
Homodimer	C138	C157	C171
	F68	Y87	F101
	A114	A133	A147
	Y116	Y135	Y149
	R136	R155	R169
	R160	R179	R193
	E184	D203	D217
LRX/RALF	F90	F109	V123
	H131	H150	H164
	E153	E172	E186
	D155	D174	D188
	D199	D218	D232
	E248	E266	E280
	E295	E313	E327
	Q296	Q314	E328
Cysteine Tail	C364	C382	C397
	C374	C392	C407
	C379	C397	C412
	C324	C253	C267
	C259	C277	C291
	C351	C369	C384
	I235	I254	I268
	Q263	E281	E295
	N326	N344	N358
	D331	E349	Q363
	N350	N368	N363
	K355	R373	R388
	R359	K377	R392
	E363	E381	E396
	N381	G399	G414
N-Glycosylations	N73	N92	N106
	N269	N287	N301
	N320	N338	N352
	N346	D364	D379

Table indicating the equivalent amino acids involved in the different interaction surfaces among LRX2, LRX8, and LRX11.